arXiv:1407.3138v1 [physics.atom-ph] 11 Jul 2014

Population trapping in bound states during IR-assisted ultra-fast photoionization of Ne^+

H.W. van der Hart and R. Morgan
Centre for Theoretical Atomic, Molecular and Optical Physics, School of Mathematics and Physics, Queen's University Belfast, Belfast, BT7 1NN, United Kingdom

(Dated: July 14, 2014)

We have investigated photoionization of Ne^+ in the combined field of a short infra-red laser pulse and a delayed ultra-short pulse of the infra-red laser's 23^{rd} harmonic. We observe an ionization yield compatible with a picture in which one electron gets excited into Rydberg states by the harmonic laser field and is subsequently removed by the infra-red laser field. Modulations are seen in the ionization yield as a function of time delay. These modulations originate from the trapping of population in low members of the Rydberg series with different states being populated at different ranges of delay times. The calculations further demonstrate that single-threshold calculations cannot reproduce the Ne^+ photoionization yields obtained in multi-threshold calculations.

PACS numbers: 32.80.Rm, 31.15.A-

I. INTRODUCTION

One of the key challenges in atomic physics is the development of techniques to monitor the motion of electrons in atoms, ions and molecules in detail. The typical timescale for electron motion is in the order of 100 attoseconds. The development of experimental techniques to produce ultra-short light pulses has been a key step towards meeting this challenge [1, 2], with current technology capable of producing pulses lasting 67 attoseconds [3].

In combination with ultra-short light pulses, the application of streaking techniques has proven to be particularly valuable in making the dynamics apparent [4]. Using the combination of both techniques, experiment has been able to investigate a range of ultra-fast processes, including measurements of relative time delays in atomic photoionization [5] and dynamics of shake-up states during high-frequency ionization of noble-gas atoms [6]. In the latter experiment, the observed dynamics is associated with dynamics within the residual ion. The ultra-fast XUV laser pulse photoionizes Ne and leaves Ne^+ in a range of excited shake-up states. The IR pulse then causes further ionization of these shake-up states, leading to double ionization. By varying the timing of the XUV pulse with respect to the IR pulse, changes in the double ionization yield are observed. These variations in the measured double ionization signal can then be associated with the interplay between the excited Ne^+ ion and the IR light field. The same process has also been studied in Kr atoms with longer excitation pulses, with an estimated duration of 24-28 fs [7]. The difference in XUV pulse length leads to subtle differences in the ionization yield. Whereas the ionization yield curves for long pulses show smooth variation as a function of time delay, in the case of ultra-fast double ionization, modulations can be noticed on top of the double ionization yields.

Several theoretical approaches have been applied to investigate ultra-fast dynamics in excitation-ionization processes, or electron dynamics in excited Rydberg series. In [6], the obtained ionization yields were analysed under the assumption that the IR field ejects the emitted electrons through tunnel ionization. Argenti and Lindroth investigated how time delays between an XUV-pulse and an IR pulse could steer ionization of He towards either the He^+ 2s or the 2p state, following excitation of the Rydberg series associated with these thresholds [8]. Dimitrovski and Madsen [9] studied the ionization of dynamics of H using few-cycle laser pulses. In this study modulations in the ionization signal were ascribed to half-cycle ionization dynamics. Kazansky and Kabachnik [10] employed a single-active-electron model for the description of the double ionization of Ne^+, where the effect of the XUV pulse was described in the sudden approximation. They also observed oscillations in the ionization yields, ascribed to quantum beats originating from coherent contributions of eigenstates of the Ne^+ ion.

In this report, we aim to investigate a similar process, IR-assisted photoionization of the Ne^+ ion, where the XUV laser pulse excites Rydberg states below the Ne^+ ionization threshold. Dynamics in the Rydberg series is then studied by varying the time delay of the XUV pulse with respect to the IR pulse. However, in order to model the dynamics in detail, we aim to have an accurate description of the Ne^+ atomic structure, as the interplay between Rydberg series associated with different thresholds may affect the ionization dynamics. Calculations of high-harmonic generation in noble-gas ions have demonstrated a factor 4 difference in the individual-atom harmonic yield obtained from an ion initially with magnetic quantum number $M = 0$ and an ion with $M = 1$ [11, 12]. This difference follows from the structure in the residual doubly charged ion. Three different thresholds lie close together, $np^4\ {}^3P^e$, ${}^1D^e$ and ${}^1S^e$. In the case of $M = 0$, emission of an electron towards the lowest ${}^3P^e$ threshold is reduced as emission of an $m = 0$ is not allowed. A second effect of the small separation between the thresholds is that the associated Rydberg series overlap. Hence, Rydberg states will have admixtures from Rydberg states associated with different ionization thresholds.

One of the approaches that can be used for the study of dynamics in atomic noble-gas ions from first principles is time-dependent R-matrix theory [13–16]. In the study of noble-gas ions, this theory was first applied to the study of two-photon ionization of Ne^+ in short high-frequency pulses, where it was demonstrated how the two-photon ionization rate can be deduced from ionization yields, when absorption of a single photon is just insufficient to achieve ionization [17]. The theory has since been applied primarily to investigate the effect of the interplay between closely spaced residual-ion thresholds on harmonic generation for Ar^+ and Ne^+ [11, 12, 18]. These studies demonstrated that the accurate description of harmonic generation requires at least inclusion of the $np^4\ ^3P^e$ and $^1D^e$ thresholds. Recently, progress has been made in the description of ultra-fast double ionization processes using time-dependent R-matrix theory [19], but at present these processes can only be described for two-electron systems.

In the present report, we apply the most recent implementation of time-dependent R-matrix theory, R-matrix including time dependence [15, 16], to study IR-assisted photoionization of Ne^+ using ultra-short light pulses. This implementation of time-dependent R-matrix theory is significantly more efficient for the exploitation of massively parallel computing facilities. This is of great assistance when dealing with IR fields, as intense long-wavelength fields require the inclusion of many angular momenta, and hence extensive basis sets. For time-dependent R-matrix approaches, this is an important consideration. The description of multiphoton processes using limited amounts of atomic structure is much more reliable when the light field is described in the length form [20]. The length form, however, necessitates the inclusion of many more angular momenta when IR fields need to be considered [21].

We will start the report with a description of the various computational techniques and basis sets used in the calculations. We will then provide Ne^+ ionization yields as a function of time delay. We then analyse the final-state wavefunction in detail, and investigate how the population of individual final states is affected by the time delay. We finish with our conclusions.

II. COMPUTATIONAL METHOD

R-matrix theory including time dependence uses the standard R-matrix approach by separating the system into two distinct regions, known as the inner region and the outer region [22]. In the inner region, all electrons are close to the nucleus. The electron-electron interactions are strong and all interactions between all electrons are therefore taken into account. In the outer region, one electron has moved away from the nucleus. For this electron, exchange interactions involving the residual-ion electrons can be neglected. This outer electron thus moves in a potential combining the long-range potential associated with the residual ion and the laser field potential.

In standard R-matrix theory the two distinct regions are connected through the so-called R-matrix [22], but in R-matrix theory including time dependence, the connection between the two regions is made through the wavefunction directly [14–16]. In the inner region, the wavefunction is described using a large configuration-interaction basis. In the outer region, the wavefunction is described using a direct product of a channel function, a residual-ion state and spin-angular functions of the continuum electron, and a grid representation of the radial wavefunction of the outer electron. The inner-region wavefunction is provided to the outer region, by extending the outer-region grid into the inner region. The inner-region wavefunction is then evaluated on this grid. This provides all the information needed by the outer region to propagate the wavefunction in the outer region. To propagate the wavefunction in the inner region, time derivatives of the outer-region wavefunction are determined at the inner-region boundary. Additional time propagators are then determined to propagate these time derivatives into the inner region.

Time propagation in the RMT approach is performed using Arnoldi propagators [23]. In the outer region, a single propagator suffices to propagate the wavefunction. In the inner region, separate Arnoldi propagators are constructed for the initial wavefunction, and for each of the time derivatives determined at the boundary [15, 16]. The number of propagators needed is given by the order of the Arnoldi propagator. In the present calculations, we use Arnoldi propagators of order 12, and a typical time step of 0.01 atomic unit. The grid spacing in the outer region is 0.08 a_0. The spatial operators are evaluated using five-point finite-difference rules. The calculations use a total of 864 processors, of which 784 are dedicated to the inner region and 80 are dedicated to the outer region. The outer region covers a total distance of over 4900 a_0.

In the inner region, Ne^+ is described by a similar wavefunction expansion as used in a previous comparison of R-matrix-Floquet theory and time-dependent R-matrix theory [17]. Following ionization of Ne^+, the residual Ne^{2+} ion can be left in three states: $2s^22p^4\ ^3P^e$, $^1D^e$ and $^1S^e$. These states are generated using an orbital set containing 1s, 2s and 2p orbitals for the Hartree-Fock ground state of Ne^{2+} [24], and additional correlation orbitals 3s, 3p, 3d, 4s, $\overline{4p}$ and $\overline{4d}$ orbitals to improve the description of the residual ion states [25]. The Ne^{2+} basis set contains the $1s^22s^22p^4$, $1s^22s2p^5$ and $1s^22p^6$ configurations and all single excitations of a 2s and 2p electron from these configurations. A small configuration-interaction calculation then provides the desired Ne^{2+} $2s^22p^4$ target states. The Ne^+ basis is generated by combining these target states with an extensive set of continuum orbitals. These continuum orbitals are generated from a B-spline basis set of 50 B-splines of order 13. The knot set spacing varies from nearly quadratic near the nucleus to nearly linear near the outer-region boundary. To improve the

description close to the nucleus, extra knot points are inserted near the nucleus. In addition, correlation orbitals are generated by combining the Ne^{2+} CI basis functions with an additional function from the orbital set. The maximum total angular momentum retained in the calculation is $L_{max} = 29$. The inner region boundary is set at 15 a_0. The energy of the lowest field-free $^2P^o$ state is adjusted to match the Ne^+ binding energy, and the energy of the lowest field-free $^2S^e$ state is also adjusted to match the literature value [26]. The reason for this shift is that the basis set for the Ne^+ states is larger compared to the one for the Ne^{2+} states. Hence the lowest Ne^+ states tend to lie too low with respect to the Ne^{2+} thresholds. The Ne^+ ground state is shifted up in energy by 0.17 eV, whereas the $2s2p^6$ state is shifted up by 0.33 eV.

In the time propagation, we do not include all field-free eigenstates obtained in the inner-region calculation. States with an energy exceeding 1345 atomic units above the first ionization threshold are excluded from the calculation. These states have rapidly oscillating wavefunctions near the nucleus and therefore are not physically relevant in the present study. However, at an energy of 1344 atomic units above the first ionization threshold, we obtain eigenstates localised at the inner-region boundary. These states acquire a large eigenvalue arising from the Bloch operator, introduced in the inner-region codes to make the inner-region Hamiltonian Hermitian [22]. These states describe aspects of wavefunction flow through the boundary, and thus need to be retained in the calculation. The RMT decides which states need to be included by monitoring the maximum boundary amplitude of each eigenstate. Within a symmetry, all states up to and including the last state with a sizable boundary amplitude are retained in the calculation, whereas all higher-lying states are excluded.

The light field consists of two laser pulses, an IR field with a wavelength of 780 nm and an XUV field involving the 23^{rd} harmonic of the IR field. Both fields last for six cycles and have a $\sin^2$ profile. The oscillating electric field has a cos-profile so that the maximum of the envelope coincides with a maximum in the electric field. After the IR pulse has finished, the wavefunction is propagated for a time corresponding to 7 cycles of the IR field. A typical profile for the electric field is shown in figure 1 for a time delay between the IR and the XUV pulse of 7.8 fs (3 optical cycles). The delay time between the pulses is defined by the onset of the $\sin^2$ profile. As a consequence figure 1 shows that, for a delay of 7.8 fs (a 3-IR-cycle delay), the maximum of the XUV excitation pulse occurs about 0.34 fs (0.13 IR-cycle) after the peak of the IR field. The peak intensity for both pulses is set to 2×10^{13} W/cm^2.

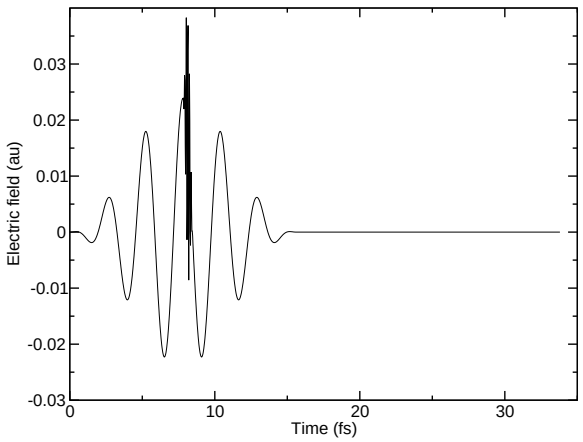

FIG. 1: Time profile of the combined electric field of the IR and the XUV pulse. The shown delay of the XUV pulse is 7.8 fs, corresponding to 3 cycles of the IR field. Since the delay is determined from the onset of the pulse, the delay means that the maximum in the XUV pulse occurs when the IR field is decreasing.

III. RESULTS AND DISCUSSION

In the present calculations, we aim to obtain ionization yields of Ne^+ in the combined field of an XUV excitation pulse into the Rydberg series, and an IR pulse, which assists the excited electron to fully escape. Since the initial excitation process involves excitation into Rydberg states, it is important to account for the possibility that the residual Ne^+ ion has been left in a highly excited state. In fact, notable fluctuations are observed in the outer-region population due to wavefunction flow from the inner region into the outer region and back. This is a clear sign that the population in Rydberg states cannot be ignored. However, we also have to take into account that the Ne^+ ion can be left in a Rydberg state associated with an excited threshold. This type of Rydberg state may autoionize, leading indirectly to photoionization. We therefore approximate the ionization yield by accounting for two different processes. When an electron is distanced further than 115 a_0 from the nucleus, it is assumed to have escaped from the residual ion. When an electron is at a distance between 15 and 115 a_0 in the outer region and in an outer-region channel associated with an excited Ne^{2+} threshold, it is assumed to be in an autoionising state, resulting in delayed, or indirect, photoionization. In order to limit the dependence of the outcomes on the final time used in the calculations, the ionization yields are averaged over the final 7.8 fs of the calculation (three cycles of the IR field).

Figure 2 shows the yields, obtained as described above, associated with photoionization and autoionization through excitation of a Rydberg state associated with an excited Ne^+ threshold. For comparison, the total population in the outer region, averaged over the

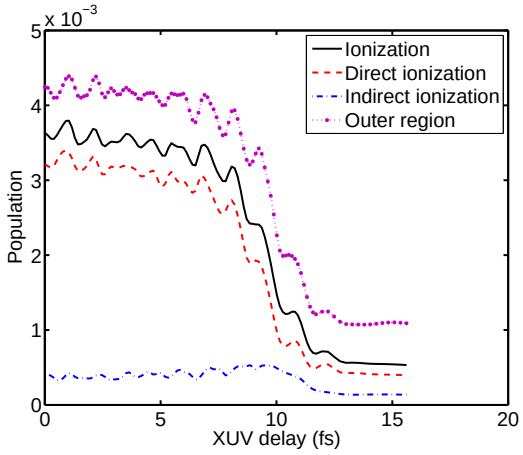

FIG. 2: (Colour online) Ne^+ ionization yield obtained as a function of time delay between the IR pulse and the XUV pulse. The XUV pulse is the 23rd harmonic of the IR pulse of 780 nm. The ionization yield (solid black line) is given by the sum of the direct ionization yield (Direct ionization, red dashed line) and the population left in Rydberg states associated with excited thresholds (Indirect ionization, blue dot-dashed line). The difference between the ionization yield and the total population in the outer region (purple dotted line with circles) can be assigned to population in Rydberg states associated with the ground-state threshold.

same final-time interval, is also shown. It can be seen that about 80% of the total population in the outer region is associated with direct ionization. A substantial fraction of the outer-region population therefore corresponds to excitation of Rydberg states. When the XUV pulse arrives prior to the peak of the IR field, about 40% of the Rydberg-state population corresponds to excited thresholds, whereas if the XUV pulse arrives when the peak of the IR field has passed, only about 20% of the Rydberg-state population corresponds to excited thresholds. The figure demonstrates that a significant fraction of the outer-region population is still confined to bound states, and that these bound states can be attached to both the ground-state threshold and to excited thresholds.

Figure 2 shows a significant variation in ionization yield as the delay of the XUV pulse is varied across the IR pulse. When the XUV pulse occurs at the tail end of the IR pulse, the total probability for ionization amounts to about 0.6×10^{-3}, whereas the total probability for ionization is a factor 6 larger when the XUV pulse occurs at the start of the IR pulse. The largest decrease in the ionization yield is seen at a delay of about 10 fs. Since this delay is well after the peak of the IR field at 7.8 fs, the peak IR intensity of 2×10^{13} W/cm^2 is more than sufficient to strip electrons from most of the Rydberg series.

One clear observation from figure 2 is that the ionization yields do not increase uniformly: for certain delay times local minima can be seen in the ionization yields. A similar behaviour was seen in the ultra-fast experiments on photoionization with excitation of Ne followed by IR photoionization of the excited Ne^+ ions. The origin of the oscillations has also been discussed theoretically, through, for example, single-active-electron calculations for model Ne^+ ions [10] and ultra-fast excitation-ionization studies of H [9]. We will now focus on the detailed final-state wavefunction to investigate the role of different atomic states in the ionization dynamics.

TABLE I: Energies of field-free states contained within the inner region with a radius of 15 a_0. Energies from the present calculations are compared with literature values [26].

State	Excitation energy Present eV	Excitation energy [26] eV
$2s^22p^5\ ^2P^o$	0	0
$2s2p^6\ ^2S^e$	26.877	26.878
$2s^22p^4(^1D)3s\ ^2D^e$	30.874	30.517
$2s^22p^4(^3P)3p\ ^2P^o$	31.597	31.485
$2s^22p^4(^1D)3p\ ^2F^o$	34.298	33.988
$2s^22p^4(^1D)3p\ ^2P^o$	34.534	34.231
$2s^22p^4(^1S)3s\ ^2S^e$	34.711	34.271
$2s^22p^4(^3P)3d\ ^2D^e$	34.800	34.727
$2s^22p^4(^3P)4p\ ^2P^o$	36.425	36.440

In order to analyse the origin of the modulations in the ionization yield, we take a more in-depth look at the final-state wavefunctions, and the coefficients associated with the field-free inner-region wavefunctions in particular. These populations are taken at the end of the calculation with no averaging. The inner-region wavefunction is described in terms of Ne^+ eigenfunctions, expressed in terms of R-matrix basis functions. If the state is relatively tightly bound, the state is well contained within the inner region, and we can estimate the final population in a particular state from its contribution to the final-state inner-region wavefunction. When the state is less tightly bound, this approach will not be appropriate as a substantial fraction of the wavefunction will extend into the outer region. For the present box size, we can use this approach for 3s and 3p outer electrons, and for 3d and 4p electrons attached to the $^3P^e$ threshold. Energies and labels of the states investigated are given in table I, and compared with reference data [26]. The differences in energy between the present data and the literature values ranges up to about 0.5 eV. The main energy difference is associated with energy differences in the residual-ion energies, with difference for states attached to the ^3Pe threshold around 0.1 eV, for states attached to the $^1D^e$ threshold around 0.35 eV, and a difference of 0.44 eV for the state attached to the $^1S^e$ threshold. To improve on these differences, even larger basis expansions for the description of Ne^{2+} are required.

The final-state populations of the field-free Ne^+ ground state and the $2s2p^6\ ^2S^e$ state has also been investigated.

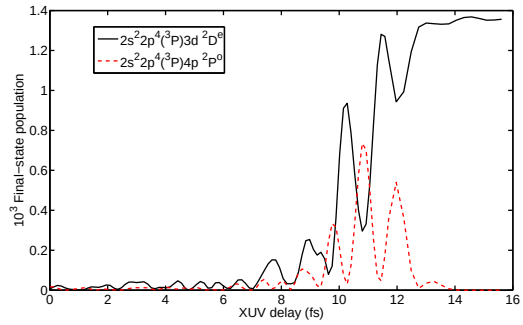

FIG. 3: (Colour online) Final-state population in $2s^22p^4(^3P^e)3d\ ^2D^e$ (black full line) and $2s^22p^4(^3P^e)4p\ ^2P^o$ (red dashed line) as a function of XUV time delay.

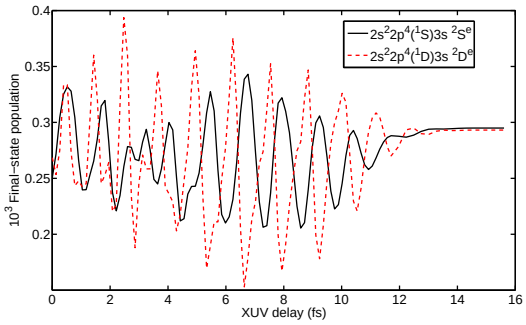

FIG. 4: (Colour online) Final-state population in $2s^22p^4(^1D^e)3s\ ^2D^e$ (red dashed line) and $2s^22p^4(^1S^e)3s\ ^2S^e$ (black solid line) as a function of XUV time delay.

For these states, however, we observe only minor variations in the final-state population as a function of XUV delay time, with fluctations of about 1.4% in the final depopulation of the ground state and fluctuations of about 3% for the final population of the $2s2p^6\ ^2S^e$ state. The lack of variation in the ground-state depopulation with respect to XUV pulse delay also means that the variation in obtained ionization yield must be reflected in a variation of population in excited states.

To illustrate how the IR field may remove population out of high-lying Rydberg states, we show in figure 3 the final-state population in $2s^22p^4(^3P^e)3d$ and $2s^22p^4(^3P^e)4p$ as a function of XUV time delay. The figure demonstrates that $2s^22p^4(^3P^e)3d$ receives about 25% of the total population that is excited by the XUV pulse. The figure demonstrates that when excitation occurs during the IR pulse, the final-state population in $2s^22p^4(^3P^e)3d$ is reduced, but this occurs not in a smooth fashion. Instead, the figure suggests that the initial step in the ionization process occurs through a coupling between $2s^22p^4(^3P^e)3d$ and $2s^22p^4(^3P^e)4p$. Since the energy gap between the states is about 1.7 eV, and hence comparable with the IR photon energy of 1.55 eV, this coupling is expected to be strong. The ionization of the $2s^22p^4(^3P^e)3d$ may thus well be governed by the ionization rate of the higher-lying $2s^22p^4(^3P^e)4p$ state. It is important to note that the figure shows final-state populations, and that the figure does not show the dynamics of the ionization process. The combined population of the two states starts to reflect the oscillations in the ionization yield, but the modulation at a delay time of 12 fs is too strong, and the modulations for delay times shorter than 8 fs are too weak.

Figure 3 suggests that the atomic structure plays a significant role in the ionization dynamics. The $2s^22p^4(^3P^e)3d$ and $2s^22p^4(^3P^e)4p$ states are strongly coupled, and population may be transferred back and forth between these states. This suggests that, for this peak IR intensity, a tunnelling picture may not give a complete description of the ionization process for low-lying states. The tunnelling picture may be appropriate for higher states in the Rydberg series, but the ionization of the $2s^22p^4(^3P^e)3d$ state appears to be enhanced resonantly by the $2s^22p^4(^3P^e)4p$ state.

The most strongly bound electron to consider in detail is the 3s electron. The final-state populations for the $2s^22p^4(^1S^e)3s\ ^2S^e$ and the $2s^22p^4(^1D^e)3s\ ^2D^e$ states are shown in figure 4. These populations remain within the range of 0.15 - 0.4×10^{-3} for all delay times. The 3s electron therefore appears too strongly bound in either state to be ionized directly by the IR laser field. However, the strong fluctuations in the final yield indicate that there is a strong coupling between these states and other states. The binding energy of the $2s^22p^4(^1S^e)3s$ is comparable to the binding energy of the $2s^22p^4(^3P^e)3d$ state, but the former does not ionize whereas the latter does. It is thus not only the total energy that is important, but also the threshold to which the electron is bound.

Figure 4 shows that the relative phase between the oscillations in the final yields for the $2s^22p^4(^1S^e)3s\ ^2S^e$ and the $2s^22p^4(^1D^e)3s\ ^2D^e$ states changes over time delay. At the longest delay times, the oscillations appear to be in anti-phase, whereas for short delays, the oscillations are in phase. The origin of these oscillations is not obvious to establish. Oscillations in anti-phase can be explained through population transfer between these states themselves. The two states are linear combinations of the same uncoupled basis states, involving a $2p^4$ core with $m_{2p} = \{-1,-1,1,1\}$ and $m_{2p} = \{-1,0,0,1\}$. A slight phase change to one component can cause oscillations in the populations of $2s^22p^4(^1S^e)3s\ ^2S^e$ and $2s^22p^4(^1D^e)3s\ ^2D^e$ state. At shorter time delays, the population of the two states is in phase. This suggests that these oscillations may be due to interactions with higher members of the Rydberg series associated with the $^1S^e$ and $^1D^e$ threshold, as this would affect both 3s states in a similar manner. Figure 4 also suggests that for time delays of 2.5 - 5 fs, dynamics involving the $2s^22p^4(^1S^e)3s\ ^2S^e$ may be especially interesting, as the oscillations are particularly rapid.

Whereas excitation of 2p electrons to the 3s and 3d states by a single photon is possible, the excitation of the

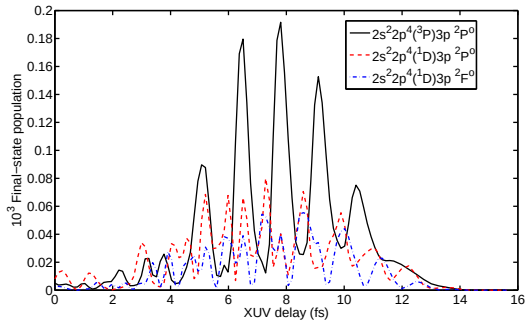

FIG. 5: (Colour online) Final-state population in $2s^22p^4(^3P^e)3p\ ^2P^o$ (solid black line), $2s^22p^4(^1D^e)3p\ ^2P^o$ (red dashed line) and $2s^22p^4(^1D^e)3p\ ^2F^o$ (blue dot-dashed line) as a function of XUV time delay.

2p electrons to the 3p states by single-photon absorption is not allowed. Nevertheless, due to the coupling between Rydberg states induced by the IR field, it is possible for the 3p states to become populated during the time propagation. Figure 5 shows the final-state populations for these states. These final-state populations tend to be strongest when the XUV delay time is near the peak of the IR field. This suggests that these states are not being tunnel-ionized by the IR field. Instead they need the IR field for population to be transferred into them. The mechanism here may be that the $2s^22p^4(^3P^e)3p\ ^2P^o$ receives an admixture of $2s^22p^4(^3P^e)3d\ ^2D^e$ due to the IR field. The XUV field excites this mixed state. The IR field is insufficiently strong to ionize this state, and when the IR pulse has finished some residual population is left behind in the $2s^22p^4(^3P^e)3p\ ^2P^o$ state.

If all the populations in these strongly bound Rydberg states are taken into account, it becomes possible to connect the modulations in the ionization yields with final-state populations in Rydberg states. At the shortest time delays, the modulations are associated with population dynamics within the 3s states. Near the peak of the IR field, low-lying 3p states can obtain an admixture of 3d states. The excitation of the 3d states can then lead to a noticeable final-state population in the 3p orbitals, removing part of the excitation spectrum out of ionization pathways. When the XUV delay increases further, the modulations become affected by interactions between states during the ionization process. Rydberg state can couple strongly, leading to population not only being driven towards higher-lying states, but also back towards lower-lying states. As a consequence, ionization may not decrease uniformly with increasing XUV time delay.

IV. CONCLUSION

In conclusion, we have used R-matrix theory including time dependence (RMT) to investigate IR-assisted photoionization of Ne^+ using ultra-short pulses. Total ionization yields as a function of time delay between the two pulses have been obtained. These yields demonstrate the fundamental nature of the ionization process as excitation by the XUV pulse, followed by removal of the excited electron by the IR pulse. The ionization yields do not increase smoothly: there are noticeable oscillations on top of the ionization yield. For a full understanding of these ionization yields, a multi-channel calculation is necessary: inclusion of just a single $2p^4$ threshold does not provide the full ionization yield.

Since the excitation of the ground state is independent of time delay, the oscillations reflect dynamics occurring between Rydberg series and differences in the populations of excited final Ne^+ states. We have demonstrated that there are significant variations in the populations of the residual Ne^+ states. The states responsible for the oscillations vary with time delay of the XUV pulse. When the XUV pulse appears early in the IR pulse, the oscillations are primarily due to 3s electrons attached to the Ne^+ thresholds, 3p electrons play a role when the IR field is at its strongest, whereas oscillations when the XUV pulse is at the tail end of the IR pulse are associated with the emission of, for example, 3d electrons due to the IR field.

The RMT approach has proven to be a suitable approach for the investigation of detailed atomic structure effects on strong-field physics. Its foundation in R-matrix theory enabled us to obtain a detailed atomic structure description of the Ne^+ ion, providing a detailed description of the Rydberg series and the interplay between the different series. This detailed description led to calculations where the inner-region description used a factor 10 more processors than the outer region. The flexibility of the RMT approach allows us to systematically improve the description of the atomic structure in the inner region, while keeping the number of channels in the outer region to a minimum.

The authors wish to thank M.A. Lysaght and L.R. Moore for their efforts in the development of the RMT codes, and J.S. Parker for valuable discussions. This research was sponsored by the Engineering and Physical Sciences Research Council (UK) under grant ref. no. G/055416/1 and through the EU Initial Training Network CORINF. This work used the ARCHER UK National Supercomputing Service (http://www.archer.ac.uk).

[1] P.M. Paul, E.S. Toma, P. Breger, G. Mullot, F. Augé, P. Balcou, H.G. Muller and P. Agostini, 2001 *Science* **292** 1689 (2001)

[2] M. Hentschel, R. Kienberger, C. Spielmann, G.A. Reider, N. Milosevic, N. Brabec, P. Corkum, U. Heinzmann, M. Drescher and F. Krausz, *Nature* **414**, 509 (2001)

[3] K. Zhao, Q. Zhang, M. Chini, Y. Wu, X.W. Wang and Z.H. Chang, *Opt. Lett.* **37**, 3891 (2012)

[4] R. Kienberger *et al*, Nature **427**, 817 (2004).

[5] M. Schultze *et al.*, Science **62**, 328 (2010).

[6] M. Uiberacker *et al.*, Nature **446**, 627 (2007).

[7] W.A. Bryan *et al*, *New J. Phys.* **14**, 013057 (2012)

[8] L. Argenti and E. Lindroth, *Phys. Rev. Lett.* **105**, 053002 (2010)

[9] D. Dimitrovski and L.B. Madsen, *Phys. Rev. A* **78**, 043424 (2008)

[10] A.K. Kazansky and N.M. Kabachnik, *J. Phys. B* **41**, 135601 (2008)

[11] A. C. Brown and H. W. van der Hart, Phys. Rev. A **88**, 033419 (2013).

[12] O. Hassouneh, A.C. Brown and H.W. van der Hart, Phys. Rev. A **89**, 033409 (2014).

[13] M. A. Lysaght, H. W. van der Hart, and P. G. Burke, *Phys. Rev. A* **79**, 053411 (2009)

[14] L.A.A. Nikolopoulos, J.S. Parker and K.T. Taylor, *Phys. Rev. A* **78**, 063420 (2008)

[15] M.A. Lysaght, L.R. Moore, L.A.A. Nikolopoulos, J.S. Parker, H.W. van der Hart and K.T. Taylor, *Quantum Dynamic Imaging: Theoretical and Numerical Methods* (eds. A.D. Bandrauk and M. Yu. Ivanov, Springer:NewYork, 2011) 107-134

[16] L.R. Moore, M.A. Lysaght, L.A.A. Nikolopoulos, J.S. Parker, H.W. van der Hart and K.T. Taylor, *J. Mod. Opt.* **58**, 1132 (2011)

[17] L. Hamonou and H.W. van der Hart, *J. Phys.B* **43**, 045601 (2010)

[18] A. C. Brown and H. W. van der Hart, Phys. Rev. A **86**, 063416 (2012).

[19] H.W. van der Hart, *Phys. Rev. A* **89**, 053407 (2014).

[20] S. Hutchinson, M.A. Lysaght and H.W. van der Hart, *J. Phys.B* **43**, 095603 (2010)

[21] E. Cormier and P. Lambropoulos, *J. Phys. B* **29**, 1667 (1996)

[22] P. G. Burke, *R-Matrix Theory of Atomic Collisions*, (Springer Verlag, Heidelberg, 2011)

[23] E.S. Smyth, J.S. Parker and K.T. Taylor, *Comp. Phys. Comm.* **114**, 1 (1998)

[24] E. Clementi and C. Roetti, *At. Data. Nucl. Data Tables* **14**, 177-478 (1974).

[25] B.M. McLaughlin and K.L. Bell, *J. Phys. B: At. Mol. Opt. Phys.* **33**, 597 (2000).

[26] A. Kramida, Yu. Ralchenko, J. Reader and NIST ASD Team (2013). *NIST Atomic Spectra Database* (ver. 5.1), [Online]. Available: http://physics.nist.gov/asd [2014, March 20]. National Institute of Standards and Technology, Gaithersburg, MD.